

Phase intergrowth and structural defects in organic metal halide Ruddlesden–Popper thin films

Naveen R. Venkatesan,[†] Rhys M. Kennard,[†] Ryan A. DeCrescent,[‡] Hidenori Nakayama,^{†, §}

Clayton J. Dahlman,[†] Erin E. Perry,[†] Jon A. Schuller,^{||} and Michael L. Chabinyc^{,†}*

[†]Materials Department, University of California, Santa Barbara, California 93106, United States

[‡]Department of Physics, University of California, Santa Barbara, California 93106, United States

[§]Electronics Materials and New Energy Laboratory, Mitsubishi Chemical Corporation,
Yokohama R&D Center 1000, Kamoshida-cho, Aoba-ku, Yokohama 227-8502, Japan

^{||}Department of Electrical and Computer Engineering, University of California, Santa Barbara,
California 93106, United States

ABSTRACT

Organic metal halide Ruddlesden–Popper phases combine the excellent optoelectronic properties of three-dimensional, bulk hybrid perovskites with superior material stability in ambient conditions. However, the thin film structure of these layered perovskites is still poorly understood, as phase purity is typically determined solely by specular X-ray diffraction. The thin film structure of these Ruddlesden–Popper phases was examined by increasingly local characterization techniques. It is difficult to assess the phase purity by purely bulk optical and diffraction measurements. From the comparison of grazing-incidence wide angle X-ray scattering (GIWAXS) patterns of cast films to expected scattering from single-crystal structures, significant in-plane disorder was observed. Spatially localized photoluminescence measurements show that films do not phase separate on the micrometer-scale. Selected area electron diffraction measurements show the intergrowth of different phases within the same thin film, consistent with previous observations seen in epitaxially-grown Ruddlesden–Popper complex oxides. Despite the presence of phase impurities that would typically be detrimental for device performance, fits to photothermal deflection spectroscopy measurements show relatively low Urbach energies of 33 meV for $(\text{C}_4\text{H}_9\text{NH}_3)_2(\text{CH}_3\text{NH}_3)_2\text{Pb}_3\text{I}_{10}$ and 32 meV for $(\text{C}_4\text{H}_9\text{NH}_3)_2(\text{CH}_3\text{NH}_3)_3\text{Pb}_4\text{I}_{13}$, indicating that the electronic properties are insensitive to the phase impurities.

INTRODUCTION

Hybrid halide perovskites have shown great promise as cost-effective, solution-processable semiconductors due to their remarkable optoelectronic properties.¹⁻⁷ Although they possess modest carrier mobilities in comparison to other inorganic semiconductors, hybrid perovskites have significantly-long carrier lifetimes,^{8,9} the origin of which is still highly debated.¹⁰⁻¹⁴ The power conversion efficiency of laboratory-scale solar cells made with mixed-cation and anion perovskite alloys have reached values near 23%,¹⁵ making perovskites competitive with existing, established thin film solar cell technologies.¹⁶ More recently, perovskite alloys have also been found to have desirable emission properties, ranging from monochromatic light for LED applications¹⁷⁻¹⁹ to broadband white light emission.²⁰⁻²² The stability of perovskite-based absorbers in the ambient environment is still a major concern, because degradation from moisture and heat are extremely detrimental to device performance.²³⁻²⁵

To improve the environmental stability of perovskites, great research efforts have been put into Ruddlesden-Popper phases, layered analogs of the three-dimensional perovskite structure.^{26,27} Extensively studied in the field of complex oxides,^{28,29} Ruddlesden-Popper phases have an overall stoichiometry of $(A')_2A_{n-1}B_nX_{3n+1}$ where n defines the size of the perovskite-like sheets that are spatially separated by the A' moieties. Formation of these phases has been achieved in hybrid perovskites through the use of a large organic (typically alkylammonium) cation as a spacer.³⁰ These spacer cations have also been utilized to produce single-crystal perovskite nanoparticles and nanoplatelets, which, due to their increased quantum confinement and phase purity, have narrow emission linewidths with large (~90%) photoluminescence quantum efficiencies.³¹⁻³³ Photovoltaic devices employing Ruddlesden-Popper phases have shown increases in their lifetimes relative to their three-dimensional counterparts.^{34,35} However, the thin film structures of these layered

perovskite films are poorly understood. Previous studies suggest that layered hybrid halide thin films naturally form highly crystalline, oriented domains upon spin coating, but optical and electronic transport measurements appear to show high defect densities which contribute to large recombination rates.^{36,37} A thorough understanding of crystalline structure within these thin films should lead to improvements in the performance of optoelectronic devices.

In this study, we characterized the thin film structure of the $n = 3$ and 4 Ruddlesden–Popper phases butylammonium methylammonium lead iodide, $(\text{C}_4\text{H}_9\text{NH}_3)_2(\text{CH}_3\text{NH}_3)_{n-1}\text{Pb}_n\text{I}_{3n+1}$, over varying length scales. Grazing-incidence X-ray scattering measurements were used to probe the average composition of thin films. Micron-scale structure was then evaluated by analyzing spatially-resolved photoluminescence maps. Transmission electron microscopy (TEM) was then used to deduce the nano-scale, local structure. Using all the structural characterization techniques, a generalized structure for Ruddlesden–Popper thin films was proposed. Finally, the impact of film structure on electronic properties was assessed by measuring the absorption coefficient with photothermal deflection spectroscopy (PDS) and fitting the absorption edges to extract the Urbach energies.

RESULTS AND DISCUSSION

To study the structure of mixed butylammonium/methylammonium (BA/MA) Ruddlesden–Popper thin films, samples were cast from solutions in *N,N*-dimethylformamide (DMF) by spin-coating onto cleaned, *z*-cut quartz substrates. Further details of growth conditions are presented in the Supporting Information Section S1. Previous studies have utilized a hot-casting technique,^{34,38–40} in which the substrate is heated prior to spinning; however, all samples here were deposited and annealed after spinning, consistent with our previous study.³⁶ A schematic depicting the general

hybrid halide Ruddlesden-Popper structure (with *n*-butylammonium spacers), along with absorbance and emission data, is shown in Figure 1. The exact absorption edges in the *n* = 3 and 4 films are difficult to discern due to scattering of long wavelength light in the measurement. The optical properties of these thin films suggest a rapid convergence to the absorbance and emission of the three-dimensionally connected MAPbI₃ for values of *n* > 2, despite the expected quantum confinement from the thickness of the lead iodide layers in the structure – in the *n* = 4 phase the inorganic layers within the structure are only approximately 2.5 nm thick. The results in Figure 1 are consistent with previously reported spectra for solution-cast thin films.^{36,38} Because measurements of exfoliated single-crystals clearly show excitonic effects and expected changes in emission with *n*, the origin of this optical behavior in thin films is still not well understood, and has been attributed to defects at the edges of crystals.³⁸

To characterize the bulk thin film structure in the *n* = 3 and 4 phases, grazing-incidence wide-angle X-ray scattering (GIWAXS) images of Ruddlesden-Popper thin films were collected and quantitatively analyzed. By utilizing a shallow incidence angle (schematic in Figure 2a), scattering from the underlying substrate is eliminated. Additionally, collection of signal by an image plate detector allows for rapid reciprocal space mapping (RSM), a technique often used on inorganic semiconductors to measure strain and lattice mismatch.^{41,42} Most importantly, the in-plane and off-specular diffraction peaks provide information about misorientation and thin film structure. GIWAXS images for (BA)₂(MA)₂Pb₃I₁₀ and (BA)₂(MA)₃Pb₄I₁₃ are presented in Figures 2c and d. Due to the fixed angle of incidence, the projection of the scattering cones onto a planar detector results in the loss of specular diffraction information, which is represented by the missing wedge of intensity along *q_z*, the out-of-plane scattering vector. These GIWAXS images can therefore be used in conjunction with specular XRD patterns (Figure S1) to map reciprocal space.

To determine whether obtained X-ray scattering patterns match expected structures, GIWAXS patterns were simulated and are shown in Figures 2e and f. Peak positions were determined from previously-solved single-crystal structures,⁴³ and the intensities of peaks were set to the square of the structure factor ($I_{hkl} = |F_{hkl}^2|$) for a particular lattice plane. Detailed descriptions of simulation calculations are provided in the Supporting Information Section S3. Additionally, peak broadening from crystals in the films was introduced to match experimental results; un-broadened spectra from a perfect crystal are presented in Supporting Information Section S4. For films exhibiting a mixture of crystalline textures, final simulated images were calculated as a linear combination of GIWAXS images corresponding to each preferred orientation direction, weighted by the associated texture fraction.

The Ruddlesden-Popper phases show differing structural disorder based on the value of n . The experimental $n = 3$ and $n = 4$ GIWAXS patterns presented here are consistent with measurements in literature on the same system.^{34,44} For comparison, measured and simulated GIWAXS patterns of the pure $n = 1$ phase are shown in Supporting Information Section S5, displaying agreement between the two images. However, in the $n = 3$ and 4 phases, it appears that many reflections are missing in the experimental patterns, noticeably along the q_{xy} direction at fixed values of q_z . To better understand the origin of these missing peaks, the schematic in Figure 2b illustrates important crystallographic directions in the structure of these Ruddlesden-Popper phases. Previous diffraction measurements have shown that the majority of the $(\text{BA})_2(\text{MA})_2\text{Pb}_3\text{I}_{10}$ and $(\text{BA})_2(\text{MA})_3\text{Pb}_4\text{I}_{13}$ align along the $[101]$ crystallographic direction, or with lead iodide sheets oriented perpendicular to the substrate.^{34,36} This implies that the measured in-plane scattering is primarily due to Bragg reflections along the $[010]$ direction, or b -axis, corresponding to the direction along which lead iodide sheets stack in the crystal structure. The presence of strong

scattering peaks at both $q_{xy} = 1.0 \text{ \AA}^{-1}$ and $q_{xy} = 2.0 \text{ \AA}^{-1}$ are consistent with those in the simulated patterns; however, the less intense $0k0$ peaks that are missing in the experimental pattern should be observable considering the intensity of the visible peaks.

To make these absences easier to observe, in-plane intensity linecuts were taken for both the experimental and simulated patterns and are shown in Figures 2g and 2h. The large spike in intensity near $q_{xy} = 0$ in the experimental patterns is due to beamstop scattering. Comparison of the expected and collected diffraction linecuts confirms the in-plane disorder seen in the two-dimensional scattering patterns, suggestive of defects in the perovskite layer stacking, possibly due to stacking faults. Quantitative fits of the scattering peaks are difficult for these thin films because broadening from crystallites causes many of the scattering peaks to overlap with each other. For analysis purposes, the full-width at half-maximum (FWHM) of the in-plane peak at $q_{xy} = 1.0 \text{ \AA}^{-1}$ is taken as a combination of two peaks as shown in Supporting Information Section S6. The scattering peak at this location was chosen as the ideal candidate for fitting as it only results from the overlap of two peaks, unlike other strong reflections that result from the overlap of three or more (Figure S4). Fits of the peaks show an approximate FWHM value of 0.03 \AA^{-1} for both $n = 3$ and 4 , indicating a minimum lateral domain size of 20.9 nm from Scherrer broadening based on our sample size and detector resolution.

Determination of the phase-purity in thin films of Ruddlesden-Popper compounds from GIWAXS is also difficult because of overlap between peaks from different phases. This issue is clear from the simulated GIWAXS pattern of three-dimensional MAPbI_3 (Figure S6) that shows overlap in its strong diffraction peaks with those in the layered phases due to the similarity in structure. Additionally, due to the similarities in the values of the a and c lattice constants in all the phases, indexing of peaks with components along the b -axis becomes the only method to

clearly distinguish between the different phases by diffraction. This makes it difficult to identify phases with larger n values in a dominantly lower n sample. Measurements at very low diffraction angles may make the differences in reflections from the layer stacking distance more apparent; however, disorder-induced peak broadening makes this challenging as the in-plane peaks fade into the background. Previous work has explored the growth kinetics of Ruddlesden–Popper thin films from solution, showing characteristic diffraction peaks associated with the different n values.^{45,46} If the phase fractions of the impurities is small, it still makes it difficult to identify in the final thin film. Therefore, X-ray scattering cannot be solely used as the means of assessing phase-purity of lead-iodide based layered perovskite thin films.

Because X-ray scattering only provides a measure of the average thin film structure, we used a combination of optical microscopy and spatial photoluminescence measurements to observe the micron-scale structure and determined that there is no phase separation on this length scale. Figures 3a and b show transmission optical microscope images of $n = 3$ and 4 thin films, respectively, illustrating distinct film morphologies. The $n = 3$ film appears to possess a larger concentration of smaller grains (~ 500 nm), while the $n = 4$ has more slender grains ($2 - 3 \mu\text{m}$) in a larger matrix of smaller (~ 500 nm) grains. To quantitatively characterize the structure, we measured the spatial dependence of the photoluminescence. Using a custom-built setup (described in Supporting Information Section S1), the localized emission from 72 square sub-regions each of size $7 \mu\text{m} \times 7 \mu\text{m}$ (optical microscope images show a fraction of the total area) were measured. These spatial emission measurements are presented in Figures 3b and c, where the average photoluminescence spectrum based on the emission from all 72 regions is shown along with the peak emission energies for both films. The average photoluminescence spectra are consistent with bulk steady-state emission measurements on films (shown in Figure 1), also confirmed by taking the difference

between the normalized steady-state spectrum and average spectrum, shown in Figure S7. The shoulders in the emission spectra also suggest local compositional deviations that are not clearly resolvable by this technique. In both cases, the peak emission energies of our thin films are blue-shifted by 90 meV in $n = 3$ and 40 meV in $n = 4$ from those presented in the earlier study,³⁸ in which both the $n = 3$ and 4 films emit at 1.7 eV. Despite this discrepancy, which could be attributed to not hot-casting films, diffraction patterns (both specular and GIWAXS) are consistent with previous studies utilizing hot-casting,^{34,44} so we are confident our thin films are structurally similar over the length scale of these optical measurements. Additionally, fitting the emission profiles to Gaussian functions (Supporting Information Section S9) shows that although the overall FWHM of the $n = 3$ film appears larger than that of $n = 4$, when decomposed into contributions from different emitters, the FWHM of the thin film states are nearly equal (0.14 eV in $n = 3$ and 0.15 eV in $n = 4$). Finally, atomic force microscope (AFM) micrographs of the two films are presented in Figures 3e and f, illustrating microscale morphologies consistent with previously reported measurements.³⁶ The micron-scale spatial photoluminescence measurements therefore show no clearly resolved phase separation in the Ruddlesden–Popper thin films.

The ambiguity in assessing phase purity from X-ray scattering and spatial emission measurements motivated the need to determine the effective stoichiometry of the final thin films. ¹H nuclear magnetic resonance (NMR) spectra were collected for both the precursor solutions and deposited films (Supporting Information Section S11), a technique that has been previously used to assess the actual stoichiometry of perovskite thin films.^{47,48} NMR spectra for the spin-coated films were obtained by scraping off material from the substrate with a razor blade and dissolving the material into deuterated dimethylsulfoxide (DMSO-*d*6). Analysis of the integrations of characteristic NMR peaks results in a measured stoichiometry of $n = 2.95 \pm 0.22$ for the $n = 3$ film

and $n = 4.20 \pm 0.39$ for the $n = 4$ film (Figure 4), so we are confident that on average, stoichiometrically, our thin films are representative of the specific layered phases. However, because some off-stoichiometric values of n are within error of our measurement, it is possible that defects of smaller and larger n values exist within our films, an assertion that has previously been suggested for phenethylammonium based Ruddlesden–Popper halides.⁴⁹ Additionally, because the spacer cation is limiting to the formation of these structures, inclusions of bulk methylammonium lead iodide (*I4/mcm* at room temperature⁵⁰) are possible when butylammonium is under-supplied.

Nanometer scale structure of the Ruddlesden-Popper thin films was characterized by transmission electron microscopy (TEM) and suggests that films contain inclusions of different n values and three-dimensional methylammonium lead iodide. To ensure consistency in the growth kinetics for TEM samples and to avoid introducing defects from utilizing a focused ion beam (FIB), we used a transfer process to examine the composition (Figure 5a). The precursor solution was first spun onto z-cut quartz substrates and the resulting films were then annealed and scraped off using a razor blade. These flakes were deposited onto TEM grids for electron microscopy measurements, similar to methods used in previous studies.^{51,52} Because this scraping method does not quantitatively preserve out-of-plane crystalline texturing, we focused only on the composition of the films on a local scale rather than on the texture. Real space TEM micrographs along with inset selected area electron diffraction (SAED) patterns for thin films of the $n = 3$ and 4 phases are shown in Figures 5b and c. The spacing of distinct sets of lattice fringes are labelled in the real space micrographs. In the $n = 3$ film, the measured d -spacing of 6.8 Å is within error of the 0 4 0 reflection of $(\text{BA})_2\text{PbI}_4$ (6.91 Å), while 3.3 Å is very similar to the spacing of the strong reflections 0 12 0 (3.28 Å), 0 16 0 (3.25 Å), and 0 20 0 (3.22 Å) in $(\text{BA})_2\text{MAPb}_2\text{I}_7$, $(\text{BA})_2(\text{MA})_2\text{Pb}_3\text{I}_{10}$, and $(\text{BA})_2(\text{MA})_3\text{Pb}_4\text{I}_{13}$, respectively. Similarly, in the $n = 4$ film, there are characteristic d -spacings of

different phases. The spacing 7.0 Å is again similar to 0 4 0 in (BA)₂PbI₄ and 6.3 Å corresponds to the 1 1 1 reflections in (BA)₂MAPb₂I₇ (6.22 Å), (BA)₂(MA)₂Pb₃I₁₀ (6.25 Å), and (BA)₂(MA)₃Pb₄I₁₃ (6.27 Å), as well as 1 1 0 in MAPbI₃ (6.25 Å). This mixed-phase behavior is further confirmed from indexing the SAED patterns (Supporting Information Section S12). Although distinct spots are visible, the diffraction patterns are fit with rings since solution growth from spin-coating results in thin films with fiber texture – there is a strong out-of-plane orientation, but crystallites are randomly rotated in-plane. Because the measured area for SAED is small, not enough grains are sampled to produce continuous rings of diffraction, but we would expect this to be true if a large area was measured. These results indicate that these films are certainly not phase pure at the nanoscale, and that inclusions of lower and higher value Ruddlesden-Popper phases are clearly forming adjacent to each other. The defects seen from TEM are also not predominantly at the crystal edges, as suggested previously for measurements on exfoliated single-crystals.³⁸ Although these literature measurements are at a much larger length scale, the nano-scale defects are also consistent with the spatial photoluminescence. With majority [101] texturing, the surface of our thin films would be made up of the edges of the Pb-I sheets, so at low emission angles, we would expect primarily edge photoluminescence. However, the oil immersion objective in our instrument allows us to collect emission over large angles, and large contributions from the single-crystal emission energies (Supporting Information Section S10) are still not present. Increased emission at the edges of the exfoliated crystals could therefore be due to phase impurities introduced by mechanical damage from the exfoliation process. Finally, the diffuse rings of intensity seen in the SAED background can be attributed to some amount of disordered phase in the films, consistent with the arcing of Bragg spots seen in GIWAXS images.

A proposed general structure of the crystalline regions of the Ruddlesden-Popper thin films is shown in Figure 6 and contains regions that correspond to the $n = 1$ through $n = 4$ phases, along with areas that are like nanoparticles of bulk MAPbI₃. This structure is a schematic of the film morphology that is consistent with both the local deviations seen in spatial photoluminescence measurements and the indexing of multiple phases from TEM. These defects are also in agreement with planar faults previously seen in epitaxially-grown inorganic Ruddlesden–Popper oxides.^{53,54} Irregular packing of the different phases is also responsible for the missing in-plane diffraction peaks from GIWAXS, since inclusions of other phases limit the amount of long-range order. Therefore, the in-plane Bragg reflections are broadened and fade into the background. The large amount of structural disorder suggests that fabricated devices should not operate efficiently, so a measure of electronic disorder is useful for comparison.

To assess the effect of structural defects and inhomogeneities on the electronic properties, high-resolution absorption spectra were collected using photothermal deflection spectroscopy (PDS) and suggest low electronic disorder in both the $n = 3$ and 4 layered compounds. Because PDS uses localized heating to measure absorbance, it is nearly insensitive to scattering effects often seen in transmission measurements, and therefore allows us to accurately measure low absorption coefficients over a wide magnitude range.^{55,56} PDS spectra of (BA)₂(MA)₂Pb₃I₁₀, (BA)₂(MA)₃Pb₄I₁₃ and bulk MAPbI₃ thin films are shown in Figure 7a. At the absorption onset, the slope of the exponential region called the Urbach tail is used as a metric to measure the amount of electronic and/or compositional disorder in semiconductors.⁵⁷ Urbach tails were fit with exponentials and are shown in the Supporting Information Section S13, giving an Urbach energy of 17 meV for MAPbI₃, consistent with 15 meV previously measured by PDS.⁵⁸ Optically accessible disorder in the density of states is captured in the slope of the true absorption onset

(Urbach tail) – increased disorder results in a shallower onset and thus an increased Urbach disorder energy. Despite appreciable structural disorder, Urbach energies of the $n = 3$ and 4 Ruddlesden-Popper films are only 33 and 32 meV, respectively, values still indicative of a reasonably large degree of electronic order. For comparison with PDS results, photovoltaic devices were fabricated to measure the external quantum efficiency (EQE), shown in Figure 7b. Assuming efficient charge extraction at the band edge, the EQE spectrum of the device should match the absorbance of the active layer and can also be fit to extract the Urbach energy. In both $n = 3$ and 4; however, the EQE is red-shifted with respect to the PDS and Urbach energies are larger, with values of 46 and 41 meV, respectively (Supporting Information Section S14).

The discrepancy between PDS and EQE measurements can be understood from the structural picture in Figure 5. Thin films are predominantly composed of the targeted n value phase – this is evident from both the distinct absorption edges in the optical data in Figure 1 as well as average n values from NMR measurements. Inclusions of higher n phases, due to their lower optical band gaps, would therefore act as funnels for photo-generated charge carriers. This transfer of excitons, or charge carriers, from smaller to larger n values has been observed in Ruddlesden–Popper thin films with a phenethylammonium spacer cation.^{18,48,59,60} As TEM analysis suggests the presence of nano-scale MAPbI₃ domains, excitations would eventually migrate to this phase during their lifetime prior to emission; this process is likely the cause of the red-shifted emission in thin films of $n = 3$ and 4. The difference in the photoluminescence peak positions between $n = 3$ (1.8 eV) and $n = 4$ (1.74 eV) is from nano-scale confinement effects of the MAPbI₃ inclusions. This energy difference depends on the size of the nanoparticles, as increased quantum confinement effects blue-shifts the emission. Because a larger amount of methylammonium is supplied in the growth of the higher n value phases, the nanoparticle domains of MAPbI₃ are on average larger in $n = 4$

films, explaining the lower energy emission in comparison to $n = 3$. Measurements of PDS and EQE differ in that the former is sensitive to all absorbing species in a sample, while the latter is dominated by the regions that generate charge from photo-excitation. In the PDS spectra presented in Figure 6, there is low-intensity signal at 1.5 eV in both the $n = 3$ and 4 traces that corresponds to a small amount of absorbing MAPbI₃ moieties. The EQE measurements are therefore biased by the presence of these MAPbI₃ nanoparticles, resulting in a red-shifted absorption onset from charge funneling. Additionally, due to the irregular distribution of these nanoparticles domains in the film, more electronic disorder is expected and is captured in the shallower slopes of the Urbach tails from EQE. Although the standalone thin film (PDS) and device (EQE) behavior could differ due to substrate effects, GIWAXS measurements of films spun on PEDOT:PSS (Figure S17) indicate that there is no appreciable structural variation between the neat thin films and those cast for device measurements. Therefore, it appears that device performance is highly dependent on the MAPbI₃ inclusions present. Furthermore, it is evident from the low Urbach energy values in PDS that the different perovskite phases present in the thin films are well-isolated from each other.

CONCLUSION

In conclusion, the thin film structure of the $n = 3$ and 4 Ruddlesden-Popper phases butylammonium methylammonium lead iodide, $(C_4H_9NH_3)_2(CH_3NH_3)_{n-1}Pb_nI_{3n+1}$, indicates significant structural disorder. GIWAXS show a significant number of missing in-plane diffraction peaks, corresponding to disorder in the stacking of the lead-iodide sheets. Additionally, micron-scale spatial mapping of the photoluminescence shows no large-scale phase separation, with only small local deviations in emission energy. To understand the source of disorder in scattering, local structure was probed by transmission electron microscopy and shows intergrowth of different

Ruddlesden–Popper phases, as well as methylammonium lead iodide. Finally, the electronic disorder was assessed by photothermal deflection spectroscopy, showing low Urbach energies of 33 and 32 meV in $(\text{BA})_2(\text{MA})_2\text{Pb}_3\text{I}_{10}$ and $(\text{BA})_2(\text{MA})_3\text{Pb}_4\text{I}_{13}$, respectively. The large amount of structural disorder coupled with the low electronic disorder suggests that lead iodide domains are electronically isolated from each other. The results suggest that studies of devices, such as solar cells and LEDs, of Ruddlesden-Popper phases should account for the presence of multiple phases in interpretation of their optoelectronic properties. Direct control over phase purity is therefore an essential goal for optimization of devices with layered perovskites.

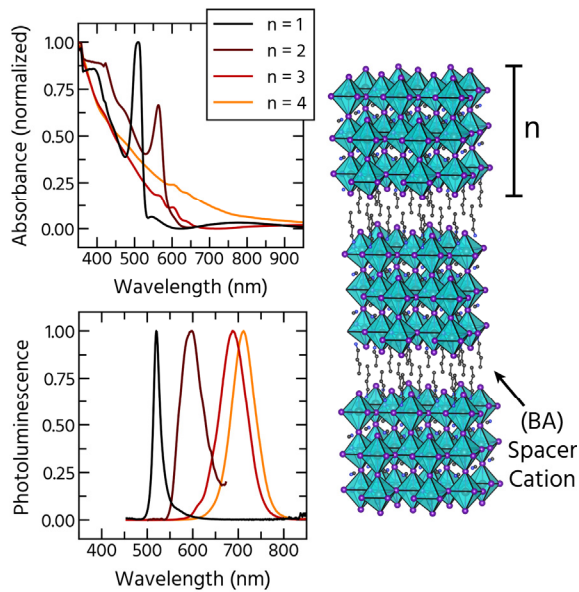


Figure 1. Normalized optical absorbance and photoluminescence for thin films of Ruddlesden-Popper phases with $n = 1$ through $n = 4$, illustrating rapid red-shifting of the emission peak and a vanishing excitonic absorption onset. A schematic of general Ruddlesden-Popper crystal structure with n value is shown on the right.

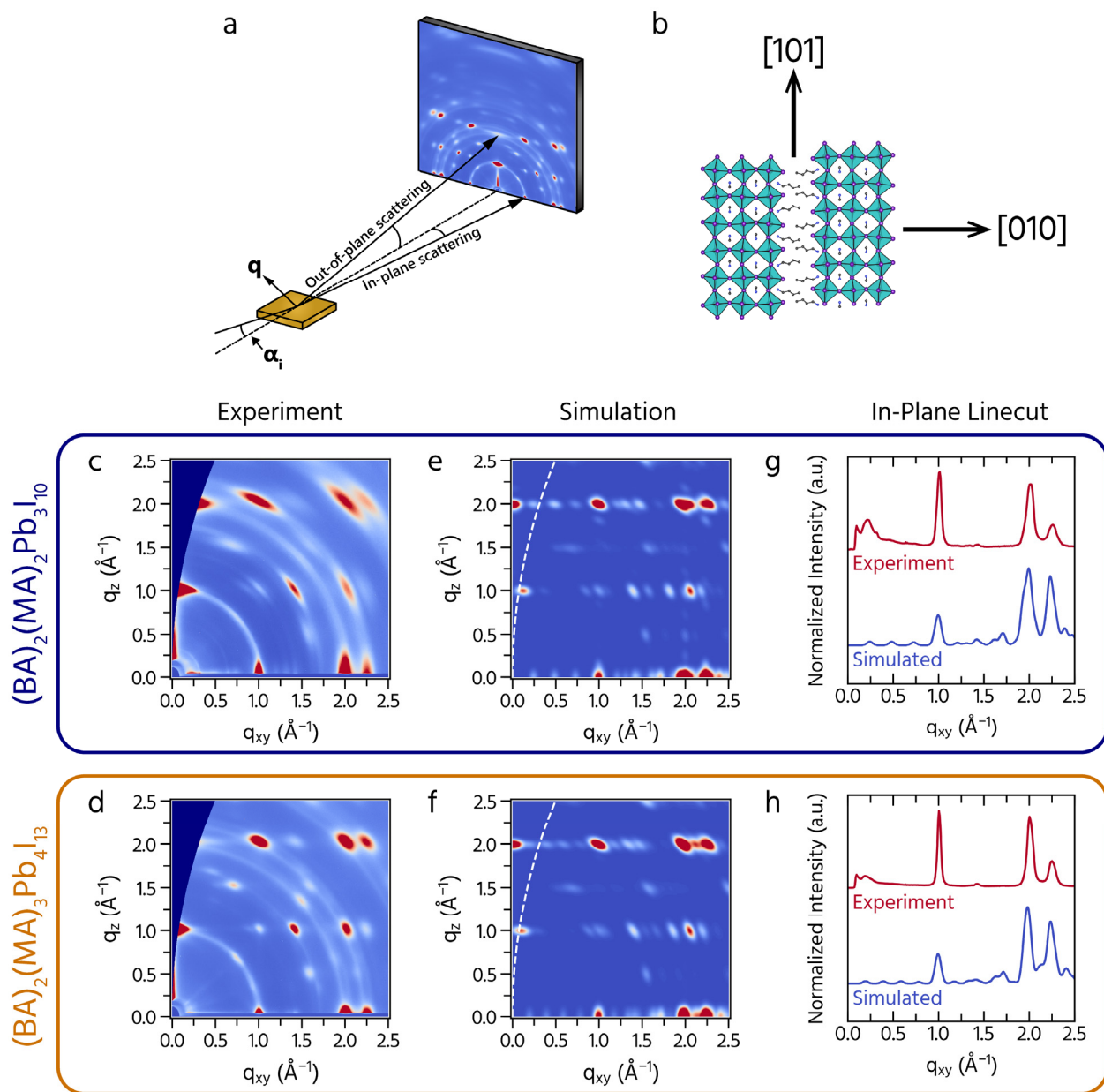


Figure 2. (a) Schematic of grazing-incidence wide-angle X-ray scattering (GIWAXS) experimental setup with image plate detector, where α_i represents the fixed, incidence angle. (b) Representative crystal structure of hybrid Ruddlesden-Popper phases ($n = 3$), showing important crystallographic directions. (c) – (d) Experimentally collected and (e) – (f) simulated GIWAXS patterns (with peak broadening based on experimental results) of $(\text{BA})_2(\text{MA})_2\text{Pb}_3\text{I}_{10}$ and $(\text{BA})_2(\text{MA})_3\text{Pb}_4\text{I}_{13}$, respectively, along with (g) – (h) linecuts of scattering intensity along the q_{xy} axis.

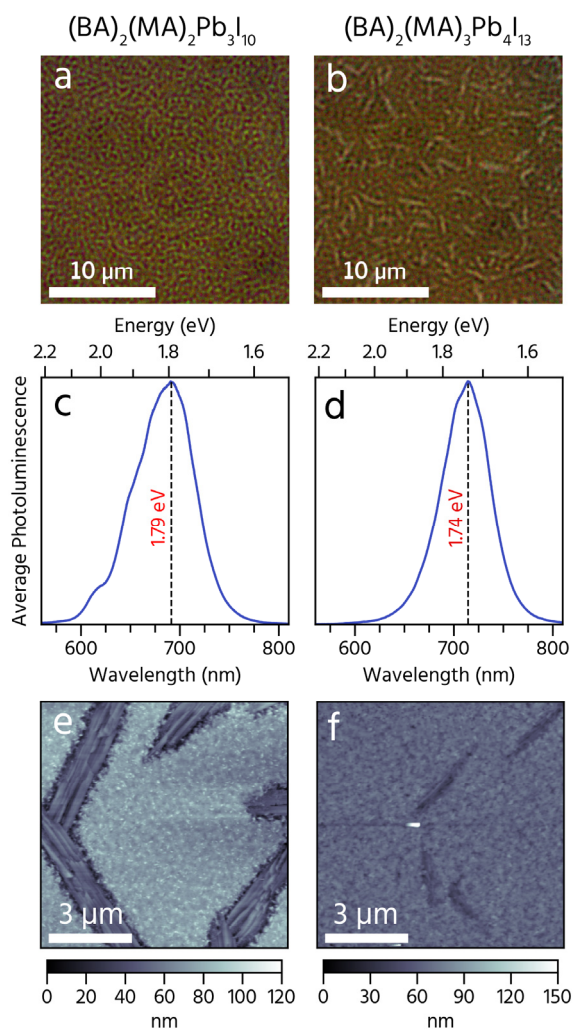


Figure 3. (a) – (b) Optical microscope images, (c) – (d) average of spatial photoluminescence spectra and peak energies, and (e) – (f) atomic force microscope (AFM) micrographs of thin films of $(\text{BA})_2(\text{MA})_2\text{Pb}_3\text{I}_{10}$ and $(\text{BA})_2(\text{MA})_3\text{Pb}_4\text{I}_{13}$, respectively. Spatial photoluminescence spectra were collected by measuring local emission of 72 regions each of size $7\ \mu\text{m} \times 7\ \mu\text{m}$. Average emission spectra match those from steady-state photoluminescence measurements. AFM micrographs are also consistent with previous measurements.

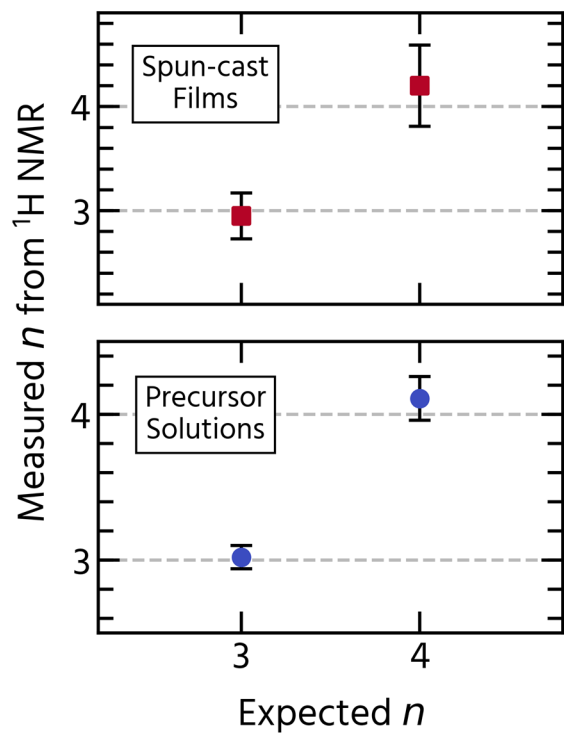


Figure 4. Experimentally measured n values of precursor solutions and spun-cast thin films of $(\text{BA})_2(\text{MA})_2\text{Pb}_3\text{I}_{10}$ ($n = 3$) and $(\text{BA})_2(\text{MA})_3\text{Pb}_4\text{I}_{13}$ ($n = 4$) from results of ^1H nuclear magnetic resonance (NMR). Error bars were determined by the standard deviation based on comparison of signals from different BA and MA protons.

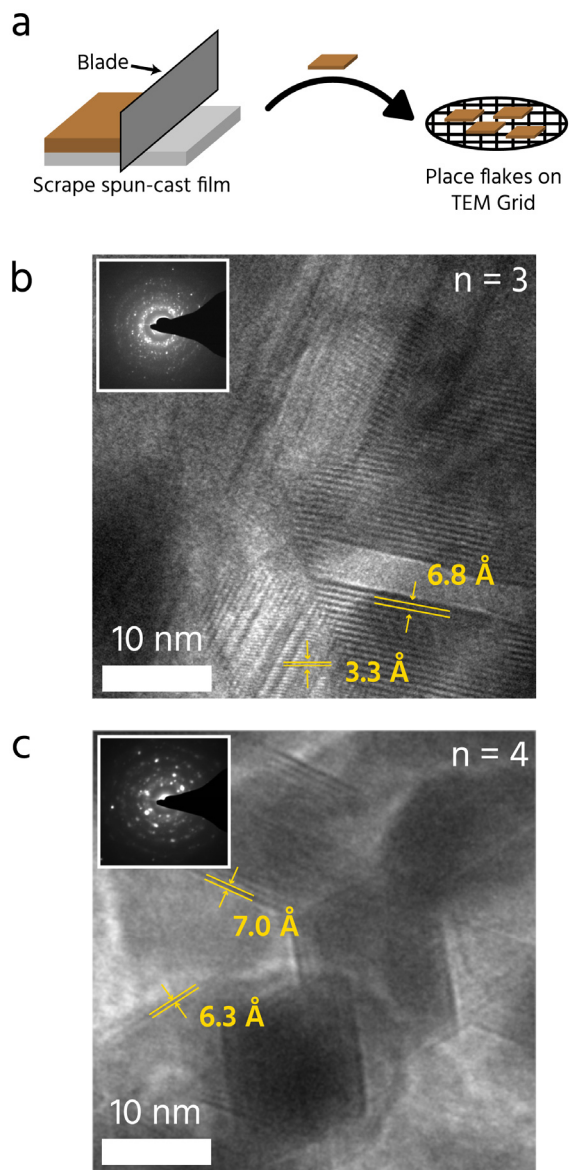


Figure 5. (a) Schematic illustrating sample preparation for transmission electron microscopy (TEM) measurements of Ruddlesden–Popper thin films, and real space TEM micrographs of (b) $(\text{BA})_2(\text{MA})_2\text{Pb}_3\text{I}_{10}$ ($n = 3$) and (c) $(\text{BA})_2(\text{MA})_3\text{Pb}_4\text{I}_{13}$ ($n = 4$), with selected area electron diffraction (SAED) patterns shown as insets. Distinct lattice fringe spacings are indicated on real space micrographs.

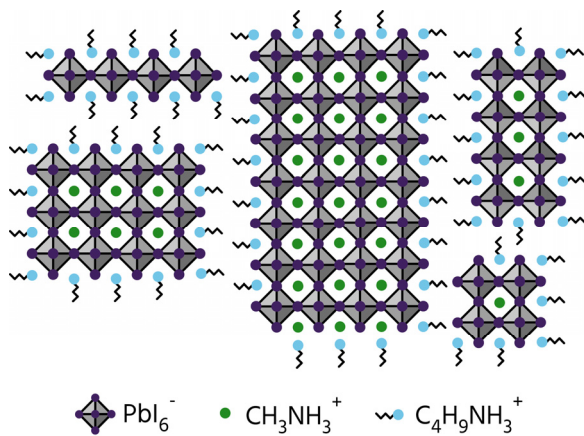


Figure 6. Proposed schematic of Ruddlesden-Popper thin film morphology, where regions appear to have structures corresponding to $n = 1$ through 4, as well as small inclusions that appears to be like nanoparticles of three-dimensional methylammonium lead iodide. Phase impurity is consistent with spatial photoluminescence and TEM, while the stacking faults are consistent with the missing in-plane peaks seen in GIWAXS.

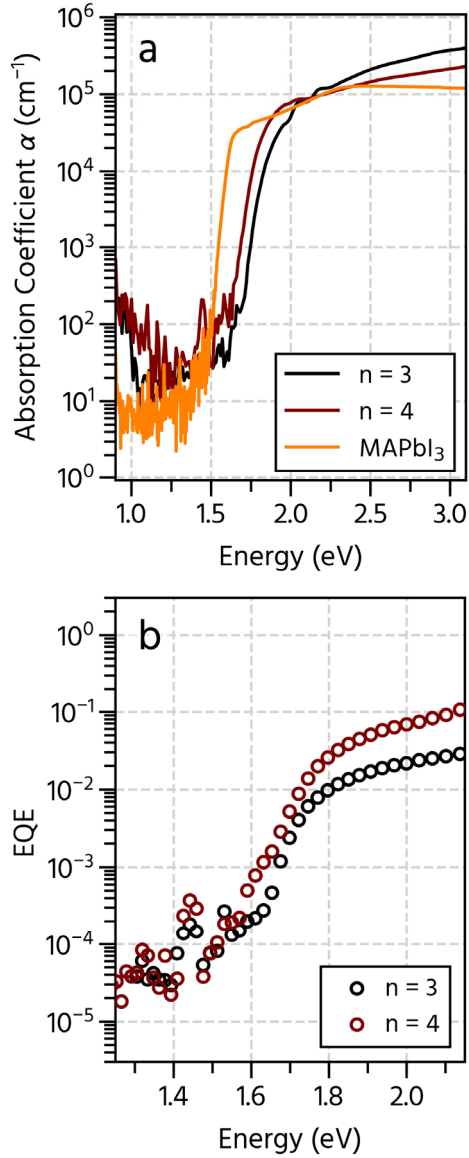


Figure 7. (a) Photothermal deflection spectroscopy (PDS) spectra of $n = 3$ and 4 Ruddlesden–Popper thin films, along with bulk methylammonium lead iodide, illustrating exponential tails at the absorption edges. (b) External quantum efficiency (EQE) spectra of devices fabricated with $n = 3$ and 4 thin films, also showing exponential tailing. Slopes of these tails are indicative of Urbach energy and degree of electronic disorder, providing information about trap states at the band edges. The red-shifted EQE with respect to the PDS is due to the presence of emitting MAPbI₃ nanoparticles to which all photo-generated charges are funneled.

SUPPORTING INFORMATION

Experimental methods describing synthesis and characterization, specular X-ray diffraction measurements, detailed description of GIWAXS simulations, diffraction peak fitting analysis, comparison of spatial and bulk photoluminescence measurements, ¹H NMR spectra of solutions and thin films, fitting of SAED patterns, and Urbach tail fits of PDS and EQE measurements.

AUTHOR INFORMATION

Corresponding Author

*Email: mchabinyc@engineering.ucsb.edu

Author Contributions

All authors have given approval to the final version of the manuscript.

Notes

The authors declare no competing financial interest.

ACKNOWLEDGMENT

Materials synthesis and structural characterization were supported by the U.S. Department of Energy, Office of Science, Basic Energy Sciences, under Award Number DE-SC-0012541. Work on devices was supported by the Defense Threat Reduction Agency under Award Number HDTRA1-15-1-0023. Use of the Stanford Synchrotron Radiation Lightsource, SLAC National Accelerator Laboratory, is supported by U.S. Department of Energy, Office of Science, Basic Energy Sciences under Contract No. DE-AC02-76SF00515. The research reported here also made use of the shared facilities of the UCSB MRSEC (NSF DMR 1720256), a member of the Materials Research Facilities Network (www.mrfn.org). R. M. K. gratefully acknowledges the National

Defense Science and Engineering Graduate Fellowship for financial support. R. A. D. and J. A. S. acknowledge support from a National Science Foundation CAREER Award, under Award Number DMR-1454260. N. R. V. gratefully appreciates the help from D. Hanifi and Prof. A. Salleo with running and analyzing PDS.

REFERENCES

- (1) Mitzi, D. B.; Chondroudis, K.; Kagan, C. R. Organic-Inorganic Electronics. *IBM J. Res. Dev.* **2001**, *45* (1), 29–45.
- (2) Berry, J.; Buonassisi, T.; Egger, D. A.; Hodes, G.; Kronik, L.; Loo, Y.-L.; Lubomirsky, I.; Marder, S. R.; Mastai, Y.; Miller, J. S.; et al. Hybrid Organic-Inorganic Perovskites (HOIPs): Opportunities and Challenges. *Adv. Mater.* **2015**, *27* (35), 5102–5112.
- (3) Kagan, C. R.; Mitzi, D. B.; Dimitrakopoulos, C. D. Organic-Inorganic Hybrid Materials as Semiconducting Channels in Thin-Film Field-Effect Transistors. *Science* **1999**, *286* (5441), 945–947.
- (4) Saparov, B.; Mitzi, D. B. Organic–Inorganic Perovskites: Structural Versatility for Functional Materials Design. *Chem. Rev.* **2016**, *116* (7), 4558–4596.
- (5) Papavassiliou, G. C.; Mousdis, G. A.; Koutselas, I. B. Some New Organic–Inorganic Hybrid Semiconductors Based on Metal Halide Units: Structural, Optical and Related Properties†. *Adv. Mater. Opt. Electron.* **1999**, *9* (6), 265–271.
- (6) Snaith, H. J. Perovskites: The Emergence of a New Era for Low-Cost, High-Efficiency Solar Cells. *J. Phys. Chem. Lett.* **2013**, *4* (21), 3623–3630.
- (7) Zhang, W.; Eperon, G. E.; Snaith, H. J. Metal Halide Perovskites for Energy Applications. *Nat. Energy* **2016**, *1* (6), 16048.
- (8) Wehrenfennig, C.; Eperon, G. E.; Johnston, M. B.; Snaith, H. J.; Herz, L. M. High Charge Carrier Mobilities and Lifetimes in Organolead Trihalide Perovskites. *Adv. Mater.* **2014**, *26* (10), 1584–1589.
- (9) Bi, Y.; Hutter, E. M.; Fang, Y.; Dong, Q.; Huang, J.; Savenije, T. J. Charge Carrier Lifetimes Exceeding 15 μ s in Methylammonium Lead Iodide Single Crystals. *J. Phys. Chem. Lett.* **2016**, *7* (5), 923–928.
- (10) Yu, Z.-G. The Rashba Effect and Indirect Electron-Hole Recombination in Hybrid Organic–Inorganic Perovskites. *Phys Chem Chem Phys* **2017**, *19* (23), 14907–14912.
- (11) Mosconi, E.; Etienne, T.; De Angelis, F. Rashba Band Splitting in Organohalide Lead Perovskites: Bulk and Surface Effects. *J. Phys. Chem. Lett.* **2017**, *8* (10), 2247–2252.
- (12) Zheng, F.; Tan, L. Z.; Liu, S.; Rappe, A. M. Rashba Spin–Orbit Coupling Enhanced Carrier Lifetime in CH₃NH₃PbI₃. *Nano Lett.* **2015**, *15* (12), 7794–7800.
- (13) Ivanovska, T.; Dionigi, C.; Mosconi, E.; De Angelis, F.; Liscio, F.; Morandi, V.; Ruani, G. Long-Lived Photoinduced Polarons in Organohalide Perovskites. *J. Phys. Chem. Lett.* **2017**, *8* (13), 3081–3086.
- (14) Zhu, X.-Y.; Podzorov, V. Charge Carriers in Hybrid Organic–Inorganic Lead Halide Perovskites Might Be Protected as Large Polarons. *J. Phys. Chem. Lett.* **2015**, *6* (23), 4758–4761.
- (15) Yang, W. S.; Park, B.-W.; Jung, E. H.; Jeon, N. J.; Kim, Y. C.; Lee, D. U.; Shin, S. S.; Seo, J.; Kim, E. K.; Noh, J. H.; et al. Iodide Management in Formamidinium-Lead-Halide–Based Perovskite Layers for Efficient Solar Cells. *Science* **2017**, *356* (6345), 1376–1379.
- (16) Polman, A.; Knight, M.; Garnett, E. C.; Ehrler, B.; Sinke, W. C. Photovoltaic Materials: Present Efficiencies and Future Challenges. *Science* **2016**, *352* (6283), aad4424.

- (17) Xiao, Z.; Kerner, R. A.; Zhao, L.; Tran, N. L.; Lee, K. M.; Koh, T.-W.; Scholes, G. D.; Rand, B. P. Efficient Perovskite Light-Emitting Diodes Featuring Nanometre-Sized Crystallites. *Nat. Photonics* **2017**, *11* (2), 108–115.
- (18) Yuan, M.; Quan, L. N.; Comin, R.; Walters, G.; Sabatini, R.; Voznyy, O.; Hoogland, S.; Zhao, Y.; Beauregard, E. M.; Kanjanaboos, P.; et al. Perovskite Energy Funnels for Efficient Light-Emitting Diodes. *Nat. Nanotechnol.* **2016**, *11* (10), 872–877.
- (19) Tsai, H.; Nie, W.; Blancon, J.-C.; Stoumpos, C. C.; Soe, C. M. M.; Yoo, J.; Crochet, J.; Tretiak, S.; Even, J.; Sadhanala, A.; et al. Stable Light-Emitting Diodes Using Phase-Pure Ruddlesden–Popper Layered Perovskites. *Adv. Mater.* **2018**, *30* (6), 1704217.
- (20) D. Smith, M.; Jaffe, A.; R. Dohner, E.; M. Lindenberg, A.; I. Karunadasa, H. Structural Origins of Broadband Emission from Layered Pb–Br Hybrid Perovskites. *Chem. Sci.* **2017**, *8* (6), 4497–4504.
- (21) Hu, T.; Smith, M. D.; Dohner, E. R.; Sher, M.-J.; Wu, X.; Trinh, M. T.; Fisher, A.; Corbett, J.; Zhu, X.-Y.; Karunadasa, H. I.; et al. Mechanism for Broadband White-Light Emission from Two-Dimensional (110) Hybrid Perovskites. *J. Phys. Chem. Lett.* **2016**, *7* (12), 2258–2263.
- (22) Smith, M. D.; Karunadasa, H. I. White-Light Emission from Layered Halide Perovskites. *Acc. Chem. Res.* **2018**, *51* (3), 619–627.
- (23) Aristidou, N.; Sanchez-Molina, I.; Chotchuangchutchaval, T.; Brown, M.; Martinez, L.; Rath, T.; Haque, S. A. The Role of Oxygen in the Degradation of Methylammonium Lead Trihalide Perovskite Photoactive Layers. *Angew. Chem. Int. Ed.* **2015**, *54* (28), 8208–8212.
- (24) Zhao, L.; Kerner, R. A.; Xiao, Z.; Lin, Y. L.; Lee, K. M.; Schwartz, J.; Rand, B. P. Redox Chemistry Dominates the Degradation and Decomposition of Metal Halide Perovskite Optoelectronic Devices. *ACS Energy Lett.* **2016**, *1* (3), 595–602.
- (25) Leijtens, T.; Eperon, G. E.; Noel, N. K.; Habisreutinger, S. N.; Petrozza, A.; Snaith, H. J. Stability of Metal Halide Perovskite Solar Cells. *Adv. Energy Mater.* **2015**, *5* (20), 1500963.
- (26) Ruddlesden, S. N.; Popper, P. New Compounds of the K_2NiF_4 Type. *Acta Crystallogr.* **1957**, *10* (8), 538–539.
- (27) Ruddlesden, S. N.; Popper, P. The Compound $Sr_3Ti_2O_7$ and its Structure. *Acta Crystallogr.* **1958**, *11* (1), 54–55.
- (28) Haeni, J. H.; Theis, C. D.; Schlom, D. G.; Tian, W.; Pan, X. Q.; Chang, H.; Takeuchi, I.; Xiang, X.-D. Epitaxial Growth of the First Five Members of the $Sr_{n+1}Ti_nO_{3n+1}$ Ruddlesden–Popper Homologous Series. *Appl. Phys. Lett.* **2001**, *78* (21), 3292–3294.
- (29) Battle, P. D.; Green, M. A.; Laskey, N. S.; Millburn, J. E.; Murphy, L.; Rosseinsky, M. J.; Sullivan, S. P.; Vente, J. F. Layered Ruddlesden–Popper Manganese Oxides: Synthesis and Cation Ordering. *Chem. Mater.* **1997**, *9* (2), 552–559.
- (30) Chen, Y.; Sun, Y.; Peng, J.; Tang, J.; Zheng, K.; Liang, Z. 2D Ruddlesden–Popper Perovskites for Optoelectronics. *Adv. Mater.* **2017**, 1703487.
- (31) Akkerman, Q. A.; D’Innocenzo, V.; Accornero, S.; Scarpellini, A.; Petrozza, A.; Prato, M.; Manna, L. Tuning the Optical Properties of Cesium Lead Halide Perovskite Nanocrystals by Anion Exchange Reactions. *J. Am. Chem. Soc.* **2015**, *137* (32), 10276–10281.
- (32) Protesescu, L.; Yakunin, S.; Bodnarchuk, M. I.; Krieg, F.; Caputo, R.; Hendon, C. H.; Yang, R. X.; Walsh, A.; Kovalenko, M. V. Nanocrystals of Cesium Lead Halide Perovskites ($CsPbX_3$, X= Cl, Br, and I): Novel Optoelectronic Materials Showing Bright Emission with Wide Color Gamut. *Nano Lett.* **2015**, *15* (6), 3692–3696.

- (33) Weidman, M. C.; Goodman, A. J.; Tisdale, W. A. Colloidal Halide Perovskite Nanoplatelets: An Exciting New Class of Semiconductor Nanomaterials. *Chem. Mater.* **2017**, *29* (12), 5019–5030.
- (34) Tsai, H.; Nie, W.; Blancon, J.-C.; Stoumpos, C. C.; Asadpour, R.; Harutyunyan, B.; Neukirch, A. J.; Verduzco, R.; Crochet, J. J.; Tretiak, S.; et al. High-Efficiency Two-Dimensional Ruddlesden-Popper Perovskite Solar Cells. *Nature* **2016**, *536* (7616), 312–316.
- (35) Liao, Y.; Liu, H.; Zhou, W.; Yang, D.; Shang, Y.; Shi, Z.; Li, B.; Jiang, X.; Zhang, L.; Quan, L. N.; et al. Highly Oriented Low-Dimensional Tin Halide Perovskites with Enhanced Stability and Photovoltaic Performance. *J. Am. Chem. Soc.* **2017**, *139* (19), 6693–6699.
- (36) Venkatesan, N. R.; Labram, J. G.; Chabinye, M. L. Charge-Carrier Dynamics and Crystalline Texture of Layered Ruddlesden–Popper Hybrid Lead Iodide Perovskite Thin Films. *ACS Energy Lett.* **2018**, *3*, 380–386.
- (37) Labram, J. G.; Venkatesan, N. R.; Takacs, C. J.; Evans, H. A.; Perry, E. E.; Wudl, F.; Chabinye, M. L. Charge Transport in a Two-Dimensional Hybrid Metal Halide Thiocyanate Compound. *J Mater Chem C* **2017**, *5* (24), 5930–5938.
- (38) Blancon, J.-C.; Tsai, H.; Nie, W.; Stoumpos, C. C.; Pedesseau, L.; Katan, C.; Kepenekian, M.; Soe, C. M. M.; Appavoo, K.; Sfeir, M. Y.; et al. Extremely Efficient Internal Exciton Dissociation through Edge States in Layered 2D Perovskites. *Science* **2017**, *355* (6331), 1288–1292.
- (39) Nie, W.; Tsai, H.; Asadpour, R.; Blancon, J.-C.; Neukirch, A. J.; Gupta, G.; Crochet, J. J.; Chhowalla, M.; Tretiak, S.; Alam, M. A.; et al. High-Efficiency Solution-Processed Perovskite Solar Cells with Millimeter-Scale Grains. *Science* **2015**, *347* (6221), 522–525.
- (40) Liao, H.-C.; Guo, P.; Hsu, C.-P.; Lin, M.; Wang, B.; Zeng, L.; Huang, W.; Soe, C. M. M.; Su, W.-F.; Bedzyk, M. J.; et al. Enhanced Efficiency of Hot-Cast Large-Area Planar Perovskite Solar Cells/Modules Having Controlled Chloride Incorporation. *Adv. Energy Mater.* **2017**, *7* (8), 1601660.
- (41) Pereira, S.; Correia, M. R.; Pereira, E.; O'Donnell, K. P.; Alves, E.; Sequeira, A. D.; Franco, N.; Watson, I. M.; Deatcher, C. J. Strain and Composition Distributions in Wurtzite InGaN/GaN Layers Extracted from X-Ray Reciprocal Space Mapping. *Appl. Phys. Lett.* **2002**, *80* (21), 3913–3915.
- (42) Saito, K.; Ulyanenkova, A.; Grossmann, V.; Rössel, H.; Bruegemann, L.; Ohta, H.; Kurosawa, T.; Ueki, S.; Funakubo, H. Structural Characterization of BiFeO₃ Thin Films by Reciprocal Space Mapping. *Jpn. J. Appl. Phys.* **2006**, *45* (9S), 7311–7314.
- (43) Stoumpos, C. C.; Cao, D. H.; Clark, D. J.; Young, J.; Rondinelli, J. M.; Jang, J. I.; Hupp, J. T.; Kanatzidis, M. G. Ruddlesden–Popper Hybrid Lead Iodide Perovskite 2D Homologous Semiconductors. *Chem. Mater.* **2016**, *28* (8), 2852–2867.
- (44) Chen, Y.; Sun, Y.; Peng, J.; Zhang, W.; Su, X.; Zheng, K.; Pullerits, T.; Liang, Z. Tailoring Organic Cation of 2D Air-Stable Organometal Halide Perovskites for Highly Efficient Planar Solar Cells. *Adv. Energy Mater.* **2017**, *7* (18), 1700162.
- (45) Zhang, X.; Munir, R.; Xu, Z.; Liu, Y.; Tsai, H.; Nie, W.; Li, J.; Niu, T.; Smilgies, D.-M.; Kanatzidis, M. G.; et al. Phase Transition Control for High Performance Ruddlesden–Popper Perovskite Solar Cells. *Adv. Mater.* **2018**, *30* (21), 1707166.
- (46) Quintero-Bermudez, R.; Gold-Parker, A.; Proppe, A. H.; Munir, R.; Yang, Z.; Kelley, S. O.; Amassian, A.; Toney, M. F.; Sargent, E. H. Compositional and Orientational Control in Metal Halide Perovskites of Reduced Dimensionality. *Nat. Mater.* **2018**, *1*.

- (47) Pareja-Rivera, C.; Solís-Camero, A. L.; Sánchez-Torres, M.; Lima, E.; Solís-Ibarra, D. On the True Composition of Mixed-Cation Perovskite Films. *ACS Energy Lett.* **2018**, *3* (10), 2366–2367.
- (48) Proppe, A. H.; Quintero-Bermudez, R.; Tan, H.; Voznyy, O.; Kelley, S. O.; Sargent, E. H. Synthetic Control over Quantum Well Width Distribution and Carrier Migration in Low-Dimensional Perovskite Photovoltaics. *J. Am. Chem. Soc.* **2018**, *140* (8), 2890–2896.
- (49) Smith, I. C.; Hoke, E. T.; Solís-Ibarra, D.; McGehee, M. D.; Karunadasa, H. I. A Layered Hybrid Perovskite Solar-Cell Absorber with Enhanced Moisture Stability. *Angew. Chem.* **2014**, *126* (42), 11414–11417.
- (50) Whitfield, P. S.; Herron, N.; Guise, W. E.; Page, K.; Cheng, Y. Q.; Milas, I.; Crawford, M. K. Structures, Phase Transitions and Tricritical Behavior of the Hybrid Perovskite Methyl Ammonium Lead Iodide. *Sci. Rep.* **2016**, *6*, 35685.
- (51) Li, M.; Wang, Z.-K.; Zhuo, M.-P.; Hu, Y.; Hu, K.-H.; Ye, Q.-Q.; Jain, S. M.; Yang, Y.-G.; Gao, X.-Y.; Liao, L.-S. Pb–Sn–Cu Ternary Organometallic Halide Perovskite Solar Cells. *Adv. Mater.* **2018**, *30* (20), 1800258.
- (52) Wang, W.; Ma, Y.; Qi, L. High-Performance Photodetectors Based on Organometal Halide Perovskite Nanonets. *Adv. Funct. Mater.* **2017**, *27* (12), 1603653.
- (53) Suzuki, T.; Nishi, Y.; Fujimoto, M. Ruddlesden–Popper Planar Faults and Nanotwins in Heteroepitaxial Nonstoichiometric Barium Titanate Thin Films. *J. Am. Ceram. Soc.* **83** (12), 3185–3195.
- (54) Suzuki, T.; Nishi, Y.; Fujimoto, M. Defect Structure in Homoepitaxial Non-Stoichiometric Strontium Titanate Thin Films. *Philos. Mag. A* **2000**, *80* (3), 621–637.
- (55) Boccara, A. C.; Fournier, D.; Jackson, W.; Amer, N. M. Sensitive Photothermal Deflection Technique for Measuring Absorption in Optically Thin Media. *Opt. Lett.* **1980**, *5* (9), 377–379.
- (56) Jackson, W. B.; Amer, N. M.; Boccara, A. C.; Fournier, D. Photothermal Deflection Spectroscopy and Detection. *Appl. Opt.* **1981**, *20* (8), 1333–1344.
- (57) Johnson, S. R.; Tiedje, T. Temperature Dependence of the Urbach Edge in GaAs. *J. Appl. Phys.* **1995**, *78* (9), 5609–5613.
- (58) De Wolf, S.; Holovsky, J.; Moon, S.-J.; Löper, P.; Niesen, B.; Ledinsky, M.; Haug, F.-J.; Yum, J.-H.; Ballif, C. Organometallic Halide Perovskites: Sharp Optical Absorption Edge and its Relation to Photovoltaic Performance. *J. Phys. Chem. Lett.* **2014**, *5* (6), 1035–1039.
- (59) Williams, O. F.; Guo, Z.; Hu, J.; Yan, L.; You, W.; Moran, A. M. Energy Transfer Mechanisms in Layered 2D Perovskites. *J. Chem. Phys.* **2018**, *148* (13), 134706.
- (60) Shang, Q.; Wang, Y.; Zhong, Y.; Mi, Y.; Qin, L.; Zhao, Y.; Qiu, X.; Liu, X.; Zhang, Q. Unveiling Structurally Engineered Carrier Dynamics in Hybrid Quasi-Two-Dimensional Perovskite Thin Films toward Controllable Emission. *J. Phys. Chem. Lett.* **2017**, *8* (18), 4431–4438.